

INTERLIBRARY LOAN

Warning: this work may be protected by the copyright laws of the United States, Title 17, United States Code.

The WSU Libraries' goal is to provide excellent customer service. Let us know how we are doing by responding to this short survey: https://libraries.wsu.edu/access services survey



Highly Efficient Polarization-Controlled Electrical Conductance Modulation in a van der Waals Ferroelectric/Semiconductor Heterostructure

Jacob Parker and Yi Gu*

Utilizing the unique in-plane/out-of-plane polarization coupling in ferroelectric van der Waals α -In₂Se₃, ferroelectric-polarization-controlled electrical conductance modulation in two-dimensional (2D) MoS₂ with a large dynamic range of over 5 orders of magnitude and excellent non-volatility is demonstrated. This highly efficient control of the electrical conductance is facilitated by enhanced capacitive coupling through atomic-layer-deposition-grown Al₂O₃ as the dielectric medium. By varying the in-plane poling bias to the ferroelectric α -In₂Se₃, the electrical conductance of vertically stacked 2D MoS₂ can be tuned continuously. This approach enables simplified device design and provides great flexibility in device integrations, and it can be applied in principle to manipulate the electronic states in any 2D semiconductors for various applications such as transistors, tunneling devices, and reconfigurable electronics. The results also provide insight into the ferroelectric polarization screening by ambient chemical species, highlighting the need for surface passivation, and/or device encapsulations.

1. Introduction

The capability to control charge carrier density is central to semiconductor-based device technologies. A common approach is to use electrostatic gating to capacitively induce n- or p-type doping, which is typically implemented by applying a vertical gate bias in a stacked metal (gate)/oxide (dielectric)/semiconductor (channel) structure, representing the basic configuration of a transistor. Recent studies have explored using the reversible spontaneous electric polarizations in oxide and polymer-based ferroelectrics to control charge carrier density in two-dimensional (2D) semiconductor-based devices.^[1–6] Particularly, the out-of-plane polarization leads to bound charges at the surface of the ferroelectric substrates, which induce opposite charges in the channel region, thereby controlling its charge density and electrical conductivity. This advantageous "gate-free" approach has several benefits including non-volatility, as no external bias

J. Parker, Y. Gu Department of Physics and Astronomy Washington State University Pullman, WA 99164, USA E-mail: yigu@wsu.edu

B

The ORCID identification number(s) for the author(s) of this article can be found under https://doi.org/10.1002/aelm.202200413.

DOI: 10.1002/aelm.202200413

Adv. Electron. Mater. 2022, 8, 2200413

is needed to maintain the polarization, simplified device fabrication processes, and enabling on-demand circuit reconfiguring through reversible ferroelectric domain patterning. [4,5] The discovery of 2D ferroelectric van-der-Waals materials, has opened up opportunities for realizing all-van-der-Waals heterostructure-based ultrathin electronics. [7–9]

Recently, α -phase In₂Se₃ (α -In₂Se₃) has emerged as a unique van der Waals ferroelectric material with interlocked out-of-plane (OOP) and in-plane (IP) polarizations. [10–16] This coupling allows for switching the OOP polarization with an IP electric field, which significantly simplifies device design, for example, by avoiding the need for fabricating both lateral and vertical electrodes, and also provides great flexibility in device integrations. [13] Recent studies have shown the possibility of using

the unique ferroelectricity of α -In₂Se₃ to control optoelectronic and electrical properties of neighboring 2D semiconductor layers. While these results represent significant milestones and provide important insight, the capability to modify channel conductivity using the OOP polarization in α -In₂Se₃ has initially been shown to be rather limited (\approx factor of 3). [17] This presents a barrier to implementation of such an approach in practical device applications.

Here, we report highly efficient and non-volatile modulation of electrical conductance in a 2D ${\sf MoS}_2$ channel, realized by enhanced capacitive coupling through atomic layer deposition (ALD)-grown Al₂O₃ as the dielectric between the channel and the ferroelectric polarizations in α -In₂Se₃. The dynamic range of the conductance modulation is over 5 orders of magnitude, representing a significant improvement compared to previous results. The corresponding high- and low-conductance states remain stable across multiple polarization switchings and also demonstrate excellent retention characteristics. Furthermore, the channel conductance can be continuously tuned by applying distinctive poling biases through lateral electrodes to α -In₂Se₃. These characteristics are particularly desirable for multi-state memory and emerging memristive applications. Our studies also provide insight into how ambient conditions influence the conductance modulation through the surface screening of ferroelectric polarizations, highlighting the need for proper surface passivation and/or device encapsulation to ensure optimal device performance.



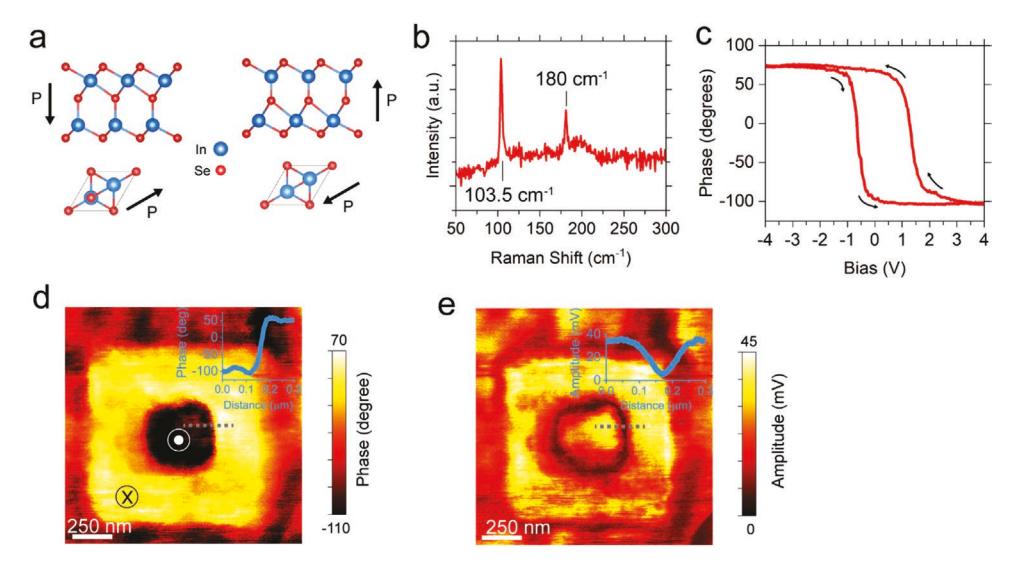


Figure 1. Ferroelectric properties of α -In₂Se₃. a) Schematic crystal structures of ferroelectric α -In₂Se₃ with opposite polarization states; b) micro-Raman spectrum of a mechanically exfoliated α -In₂Se₃ layer; c) OOP phase hysteresis loop measured on a 30-nm-thick α -In₂Se₃ layer; OOP d) phase and e) amplitude maps of a 33-nm-thick α -In₂Se₃ layer with the outer (inner) square area poled by an AFM probe biased at +3.5 V (–3.5 V). The insets to (d) and (e) show the line profiles of phase and amplitude across opposite domains, respectively.

2. Results and Discussion

Figure 1a shows the schematic crystal structures of α -In₂Se₃ in different polarization states.^[10] The interlocked OOP and IP polarizations arise from symmetry-breaking positions of the central Se atom layer in both OOP and IP directions. Unlike conventional oxide ferroelectrics, [19] these polarizations are sustained by strong covalent bonds, [10,20] leading to robust ferroelectricity stable above room temperature.[12,14,21] Figure 1b shows a micro-Raman spectrum of a mechanically exfoliated α -In₂Se₃ layer, where the main phonon peaks at \approx 103.5 and 180 cm⁻¹ correspond to a sum of two E modes (i.e., a combination mode) and an A_1 mode, respectively, in the α -phase lattice.[22] To confirm the ferroelectric properties in as-prepared α-In₂Se₃ layers, piezoresponse force microscopy (PFM) with local poling provided by a biased atomic force microscope (AFM) probe was conducted. The 180° change in the piezoresponse phase (Figure 1c) corresponds to the reversal of the OOP polarization under the external electric field, and the phase hysteresis loop, characteristic of ferroelectricity, shows two opposite remnant polarization states with the coercive electric field estimated to be $\approx 300 \text{ kV cm}^{-1}$. We note that the phase hysteresis loop is off-centered with regard to the poling bias axis, which can be attributed to the work function difference between the AFM tip and α -In₂Se₃.^[11] The biased AFM probe was also used to pole the local polarizations in defined areas. The probe was first biased at + 3.5 V and was scanned in contact mode over a square area (1 × 1 μ m) on a 33-nm-thick α -In₂Se₃ layer. As the tip bias exceeds the coercive voltage, this defines the area of OOP polarization that points into the layer (x). The probe bias was then switched to -3.5 V and scanned across a smaller box $(0.25 \times 0.25 \,\mu\text{m})$ that overlaps with the previously defined area, leading to an out-of-layer OOP polarization (·). This "boxin-box" pattern that features ≈150° OOP polarization direction difference is visualized by PFM phase mapping (Figure 1d and inset). Additionally, the amplitude map (Figure 1e and inset) shows minimal piezoresponse at the boundary between two boxes, as expected with the location of the domain wall, which does not possess a ferroelectric polarization.

To demonstrate the OOP-IP polarization coupling, particularly control of the OOP polarization states using an IP electric field, we first investigate the electrical properties of α -In₂Se₃ devices with poling biases applied through lateral electrodes, which supports an IP field, as shown in Figure 2a. The current voltage ($|I_d|$ vs V_{ds}) relation (Figure 2b) shows pinched hysteresis loops that expand with the increasing sweeping range of $V_{\rm ds}$. Such a behavior is characteristic of memristive switching, and can be attributed to the evolution of ferroelectric OOP polarizations and domains due to the changing external IP electric field.^[23] We further probe the influence of the IP field on the OOP polarization states by PFM phase mapping. Particularly, the device channel was subject to lateral poling using biasing pulses with opposite polarity (±20 V with 15 s duration). Structural phase transitions can be ruled out as the main phonon modes of the α -In₂Se₃ lattice remain intact (Figure 2c). The PFM phase maps after each poling biasing pulse show distinctive changes in the OOP polarization states (Figure 2d,e), confirming control of the OOP polarization by the external IP field. We note that the changes in the OOP phase angle are less than 180° between Figure 2d,e, which is most likely due to the rather low IP poling electric field (≈24 kV cm⁻¹) as compared to the coercive electric field shown in Figure 1c, leading to imperfect OOP polarization reversal. In addition, the domain nucleation dynamics and domain wall motions are sensitive to local defects, which may contribute to the spatially non-uniform OOP polarization phase changes observed across the device. This spatial inhomogeneity, however, is an important underlying mechanism for the observed memristive behavior of α-In₂Se₃ layers, specifically the continuously tunable electrical resistance.^[23]

The OOP polarization generates surface bound charges on α -In₂Se₃, the polarity of which can be switched by reversing

www.advancedsciencenews.com

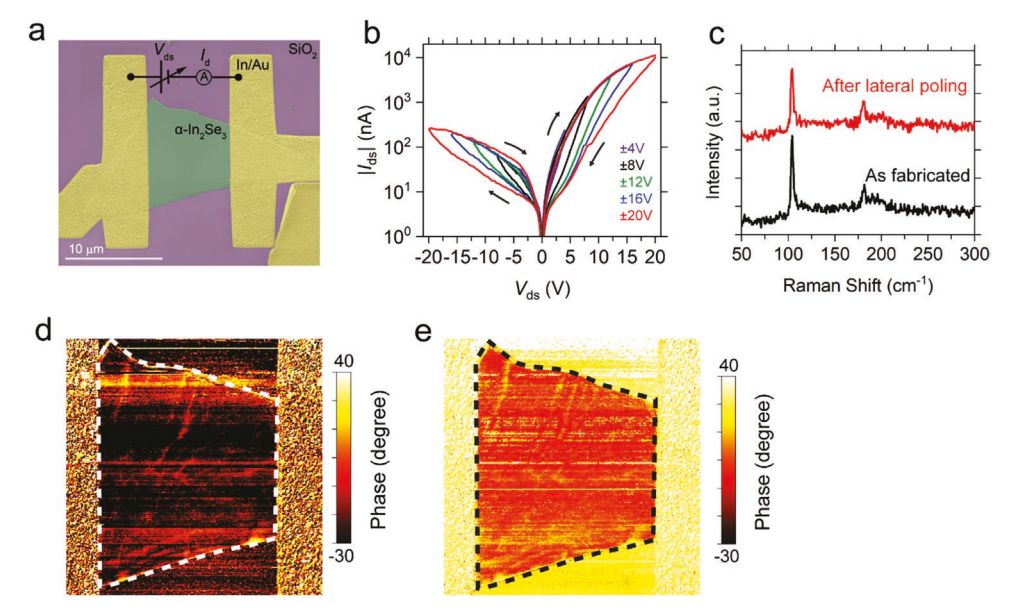


Figure 2. OOP polarization in α -In₂Se₃ controlled by an IP electric field. a) SEM (false color) image of an α -In₂Se₃ device with lateral electrodes; b) $|I_d|$ versus V_{ds} relations of a similar device under expanding V_{ds} sweeping ranges with the arrows indicating the sweeping direction; c) Raman spectra of another similar device before and after poling with a lateral bias pulse of 20 V with 15 s duration; OOP-PFM maps of the device shown in (a) subject to a lateral poling biasing pulse of d) +20 V and e) -20 V with 15 s duration.

the polarization with a lateral bias as shown above. Through capacitive coupling, these surface bound charges can induce opposite charges in the overlaying semiconductor channel material, providing the ability to control the channel conductance. **Figure 3**a,b shows the schematic device structure that

implements this non-volatile "ferroelectric charging" concept and an SEM image of a typical device, respectively. Particularly, multilayer (\approx 6 nm thick) MoS₂ is the active channel, and α -In₂Se₃ is the ferroelectric, with a 6–10 nm-thick Al₂O₃ layer grown by ALD sandwiched between the MoS₂ and α -In₂Se₃

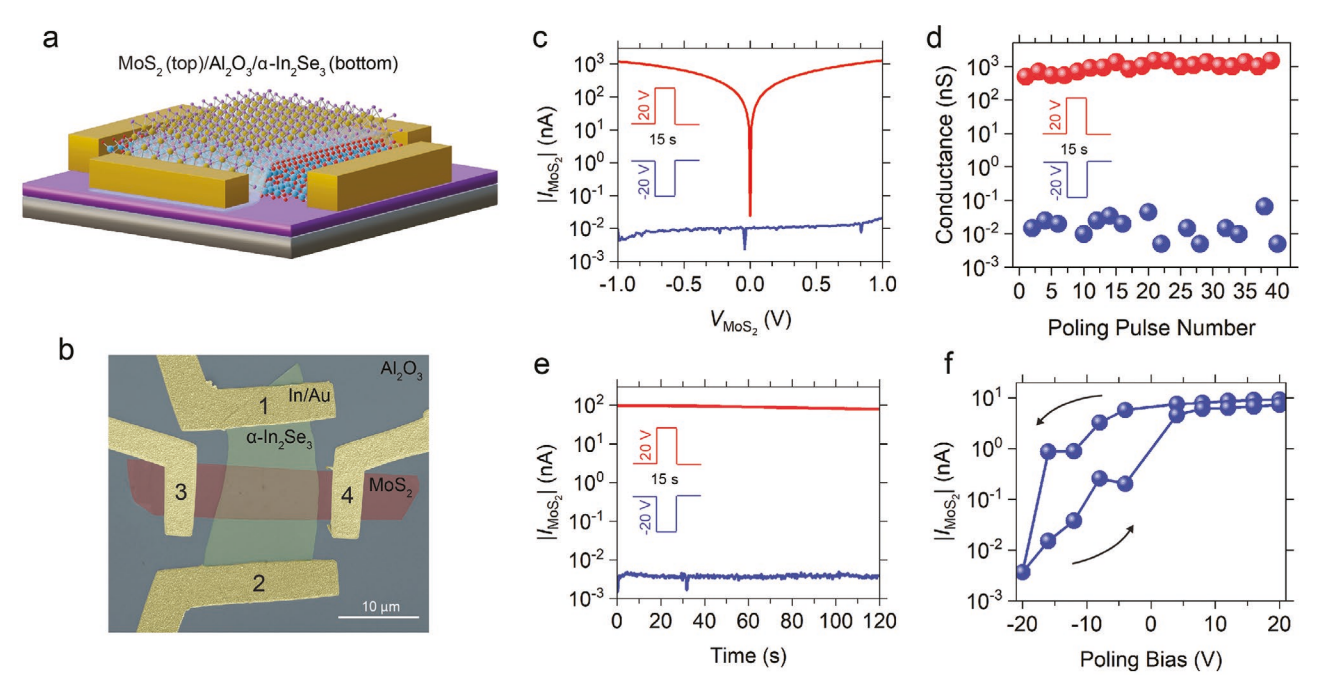


Figure 3. Polarization-controlled electrical conductance modulation characteristics measured in a high-purity Ar environment. a) Schematics and b) SEM (false color) image of a $MoS_2/Al_2O_3/\alpha$ - In_2Se_3 heterostructure device; c) $|I_{MoS2}|$ versus V_{MoS2} relations after the ferroelectric α - In_2Se_3 was subject to lateral poling with ± 20 V pulses with 15 s duration; d) MoS_2 channel conductance modulation over 40 lateral poling voltage pulses; e) I_{MoS2} (measured at $V_{MoS2} = 100$ mV) for the high-/low-conductance states as a function of time; f) I_{MoS2} (measured at $V_{MoS2} = 100$ mV) as a function of the lateral poling bias with the arrows indicating the bias sweeping direction.

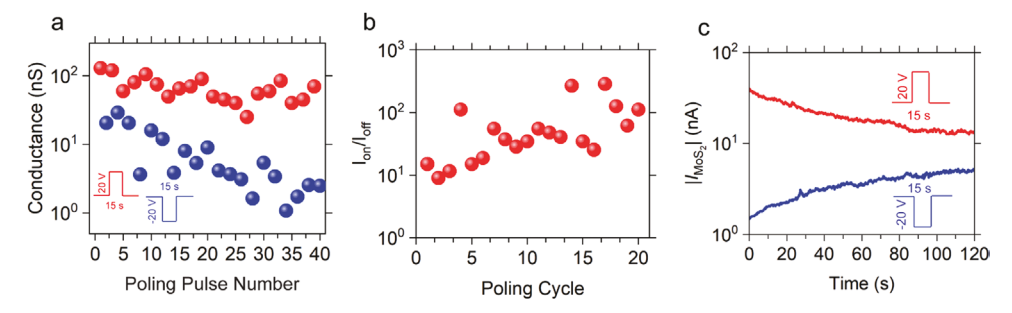


Figure 4. Polarization-controlled electrical conductance modulation characteristics measured in ambient air. a) MoS₂ channel conductance modulation over 40 lateral poling voltage pulses; b) MoS₂ channel current on/off ratio (I_{on}/I_{off} , measured at $V_{MoS2} = 500$ mV) measured over 20 cycles of lateral poling; c) I_{MoS2} (measured at $V_{MoS2} = 1$ V) for the high-/low-conductance states as a function of time.

to improve the capacitive coupling. Voltage poling pulses with opposite polarity (±20 V pulses with 15 s duration) were applied across the electrodes 1-2 to tune the OOP polarization in α -In₂Se₃; after each poling, the electrodes 1–2 were disconnected from the circuit (i.e., no external bias to α -In₂Se₃), and all the following electrical measurements of the MoS₂ channel, including the current-voltage ($|I_{MoS2}|$ vs V_{MoS2}) relation and the corresponding electrical conductance, were then measured in a high purity Ar environment. As shown in the $|I_{MoS2}|$ versus V_{MoS2} plots (Figure 3c), the changes in I_{MoS2} after poling the underlying α -In₂Se₃ layer are larger than 5 orders of magnitude, with the positive (negative) poling bias corresponding to electron accumulation (depletion), i.e., n-(p-) type doping in the n-type MoS₂ channel. This remarkable modulation of the MoS₂ channel conductance remains robust over multiple poling of α -In₂Se₃ (Figure 3d). The non-volatile nature of the high- and low-conductance states of the MoS₂ channel, corresponding to the opposite polarization states in the ferroelectric α-In₂Se₃, is demonstrated through the excellent retention behaviors shown in Figure 3e. Furthermore, by varying the poling bias magnitude, which in turn modifies the ferroelectric domain configurations, [23] the MoS₂ channel conductance can be tuned continuously (Figure 3f) within a large dynamic range (more than 3 orders of magnitude). The hysteretic behavior of the MoS2 channel conductance as a function of the α-In₂Se₃ poling bias confirms the ferroelectric charging as the underlying mechanism. The hysteresis loop is, however, much off-centered with regard to the zero poling bias. We note that positive fixed oxide charges are present in AlO_x layers, [24] and these charges effectively introduce n-type doping[25] in the MoS2 channel. A larger negative poling bias to α -In₂Se₃, which induces p-type doping, is therefore required to overcome such an effect.

The ferroelectric charging effect is determined by surface bound charge density in $\alpha\text{-In}_2\text{Se}_3$. Previous theoretical studies have indicated an OOP electric dipole moment of \approx 0.1 eÅ per unit cell in $\alpha\text{-In}_2\text{Se}_3$. [10] With the in-plane lattice constant of \approx 4.1 Å, [10] the surface bound charge density of a monolayer $\alpha\text{-In}_2\text{Se}_3$ can be estimated to be on the order of \approx 10¹² cm⁻². Assuming no surface charge screening and perfect capacitive coupling, this would point to an induced charge density of the same order of magnitude inside the MoS₂ channel. However, from the experimental $|I_{\text{MoS}2}|$ versus $V_{\text{MoS}2}$ relations, the induced charge density can be estimated to be only \approx 10¹⁰ cm⁻². This indicates that the surface bound charges are

largely screened/compensated, which is in fact beneficial for minimizing the depolarization field and is consistent with the stable polarization states in $\alpha\text{-In}_2\text{Se}_3$ that provide the non-volatility of conductance modulation shown in Figure 3e. There are multiple potential mechanisms for surface charge screening. Specifically, both free charge carriers in $\alpha\text{-In}_2\text{Se}_3$, which is an n-type semiconductor, $^{[26]}$ and the aforementioned oxide charges in the ALD-grown Al $_2\text{O}_3$ can provide a screening effect. In addition to these material-intrinsic mechanisms, another important, extrinsic process is charge neutralization by the surface-adsorbed chemical species such as water and hydroxyl groups in ambient environment. $^{[27]}$

As all the conductance modulation measurements shown in Figure 3 were conducted in the Ar environment, it is expected that the surface adsorption of charged ions is minimal. On the other hand, this process can become significant in ambient air due to the abundance of water vapor. This is confirmed by the results obtained in ambient air shown in Figure 4. The dynamic range of the channel conductance modulation (Figure 4a,b), while still significant, decreases to ≈1 to 2 orders of magnitude as shown in the ratio between the currents in the high- and low-conductance states ($I_{\rm on}/I_{\rm off}$). The retention test of the MoS2 channel current shows that the high- and lowconductance states converge toward each other initially, corresponding to a decay in the dynamic range, and then become stable after ≈100 s. This slow stabilization is presumably due to the redistribution of surface-adsorbed chemical species in response to the changes in the ferroelectric domain configurations and associated OOP polarizations. While further studies are required to elucidate the underlying mechanisms and adsorption kinetics, these results indicate that proper surface passivation and/or device encapsulation might be necessary to preserve the efficient conductance modulation.

3. Conclusion

In summary, by utilizing the unique in-plane/out-of-plane polarization coupling in ferroelectric van der Waals $\alpha\text{-In}_2\text{Se}_3$, we demonstrate ferroelectric-polarization-controlled electrical conductance modulation in 2D MoS $_2$ with a large dynamic range of over 5 orders of magnitude and excellent non-volatility. Furthermore, the electrical conductance in MoS $_2$ can be tuned continuously by varying the in-plane poling bias to $\alpha\text{-In}_2\text{Se}_3$. This approach allows for simplified device design with great



www.advancedsciencenews.com



flexibility in device integration, and can be applied to any 2D channel materials to control the electronic states in these materials for various applications such as transistors, tunneling devices, and reconfigurable electronics. Our results also provide initial insight into the ferroelectric polarization screening by ambient chemical species, highlighting the need for surface passivation and/or device encapsulations.

4. Experimental Section

Device Fabrication: Bulk α-In₂Se₃ and MoS₂ crystal was purchased from 2D Semiconductors Inc. α-In₂Se₃ crystal flakes were mechanically exfoliated from the bulk crystal and subsequently transferred by a PDMS film (PF-60-X4, GelPak) to 90 nm SiO₂/Si substrates (University Wafer). Metallic electrodes of In/Au (50/80 nm) were patterned by e-beam lithography and deposited by physical vapor deposition (Nexdep, Angstrom Engineering) at a pressure of $2-5\times10^{-7}$ Torr with the deposition rate of 1 and 0.4 Å s⁻¹, respectively. A thin layer of Al₂O₃ was then patterned by e-beam lithography and deposited by atomic layer deposition (Savannah, Ultratech) at 150 °C using Al(CH₃)₃ and H₂O as precursors and pulse time of 15 ms for both precursors. Ultrathin MoS₂ crystal flakes were then mechanically exfoliated from the bulk crystal and transferred by a PDMS film onto the α -In₂Se₃/Al₂O₃ heterostructure. In/ Au metal electrodes with thicknesses of 50/80 nm were then patterned on the MoS₂ by e-beam lithography and deposited by physical vapor deposition.

AFM Characterization: All AFM measurements were performed under ambient condition on a Bruker Dimension Icon atomic force microscope. Conductive probes (ATEC) with a PtIr5 coating and average spring constant of 2.8 N m⁻¹ were used for topography and PFM measurements. The OOP contact resonant frequency and IP contact resonant frequency for PFM measurements was ≈245–285 and 795 kHz respectively. Scanning rates of 0.35–0.75 Hz were utilized for the tip scanning frequency in all measurements. For PFM phase and amplitude hysteresis measurements, conductive probes (Bruker) with PtIr coating and average spring constant of 0.1 N m⁻¹ were used.

Raman Spectroscopy: Raman measurements were performed using a 633-nm He–Ne laser and a confocal Raman microscope (InVia, Renishaw) equipped with a $100\times$, NA = 0.7 objective (Nikon). Spectra were taken using a laser power of ≈ 0.3 mW and an accumulation time of 240 s.

Electrical Characterization: Electrical measurements were performed at room temperature using a Keysight B2902A precision source/meter unit. For measurements in an Ar environment, samples were mounted inside a heating/cooling stage (Instec, HCS302) under a continuous flow of ultrapure (99.999%) Ar.

Acknowledgements

This work was supported by U.S. National Science Foundation (CMMI-1930769). The authors would like to thank Prof. Hanwei Gao's group at Florida State University for preliminary trials of the ALD process, and Prof. Brian Collins at Washington State University for access to the physical vapor deposition system. The e-beam lithography was conducted at the Franceschi Microscopy and Imaging Center at Washington State University. The ALD was conducted in the microfabrication cleanroom at the Institute of Materials Research at Washington State University. [Correction added after publication 09 September 2022: Fig. 3 has been replaced]

Conflict of Interest

Y.G. has equity interest in Klar Scientific.

Data Availability Statement

The data that support the findings of this study are available from the corresponding author upon reasonable request.

Keywords

ferroelectrics, two-dimensional materials, electrical properties, van der Waals heterostructures

> Received: April 12, 2022 Revised: May 31, 2022 Published online: June 30, 2022

- [1] J. W. Chen, S. T. Lo, S. C. Ho, S. S. Wong, T. H. Y. Vu, X. Q. Zhang, Y. D. Liu, Y. Y. Chiou, Y. X. Chen, J. C. Yang, Y. C. Chen, Y. H. Chu, Y. H. Lee, C. J. Chung, T. M. Chen, C. H. Chen, C. L. Wu, Nat. Commun. 2018, 9, 3143.
- [2] Y. Chen, X. D. Wang, P. Wang, H. Huang, G. J. Wu, B. Tian, Z. C. Hong, Y. T. Wang, S. Sun, H. Shen, J. L. Wang, W. D. Hu, J. L. Sun, X. J. Meng, J. H. Chu, ACS Appl. Mater. Interfaces 2016, 8, 32083.
- [3] A. Lipatov, T. Li, N. S. Vorobeva, A. Sinitskii, A. Gruverman, *Nano Lett.* 2019, 19, 3194.
- [4] L. Lv, F. W. Zhuge, F. J. Xie, X. J. Xiong, Q. F. Zhang, N. Zhang, Y. Huang, T. Y. Zhai, Nat. Commun. 2019, 10, 3331.
- [5] G. J. Wu, B. B. Tian, L. Liu, W. Lv, S. Wu, X. D. Wang, Y. Chen, J. Y. Li, Z. Wang, S. Q. Wu, H. Shen, T. Lin, P. Zhou, Q. Liu, C. G. Duan, S. T. Zhang, X. J. Meng, S. W. Wu, W. D. Hu, X. R. Wang, J. H. Chu, J. L. Wang, Nat. Electron. 2020, 3, 43.
- [6] Z. Y. Xiao, J. F. Song, D. K. Ferry, S. Ducharme, X. Hong, Phys. Rev. Lett. 2017, 118, 236801.
- [7] X. X. Jiang, X. B. Hu, J. H. Bian, K. Zhang, L. Chen, H. Zhu, Q. Q. Sun, D. W. Zhang, ACS Appl. Electron. Mater. 2021, 3, 4711.
- [8] M. W. Si, P. Y. Liao, G. Qiu, Y. Q. Duan, P. D. D. Ye, ACS Nano 2018, 12, 6700.
- [9] X. W. Wang, C. Zhu, Y. Deng, R. H. Duan, J. Q. Chen, Q. S. Zeng, J. D. Zhou, Q. D. Fu, L. You, S. Liu, J. H. Edgar, P. Yu, Z. Liu, Nat. Commun. 2021, 12, 1109.
- [10] W. J. Ding, J. B. Zhu, Z. Wang, Y. F. Gao, D. Xiao, Y. Gu, Z. Y. Zhang, W. G. Zhu, Nat. Commun. 2017, 8, 14956.
- [11] Y. Zhou, D. Wu, Y. H. Zhu, Y. J. Cho, Q. He, X. Yang, K. Herrera, Z. D. Chu, Y. Han, M. C. Downer, H. L. Peng, K. J. Lai, *Nano Lett.* 2017, 17, 5508.
- [12] J. Xiao, H. Y. Zhu, Y. Wang, W. Feng, Y. X. Hu, A. Dasgupta, Y. M. Han, Y. Wang, D. A. Muller, L. W. Martin, P. A. Hu, X. Zhang, Phys. Rev. Lett. 2018, 120, 227601.
- [13] F. Xue, X. He, J. R. D. Retamal, A. L. Han, J. W. Zhang, Z. X. Liu, J. K. Huang, W. J. Hu, V. Tung, R. H. He, L. J. Li, X. X. Zhang, Adv. Mater. 2019, 31, 1901300.
- [14] F. Xue, W. J. Hu, K. C. Lee, L. S. Lu, J. W. Zhang, H. L. Tang, A. Han, W. T. Hsu, S. B. Tu, W. H. Chang, C. H. Lien, J. H. He, Z. D. Zhang, L. J. Li, X. X. Zhang, Adv. Funct. Mater. 2018, 28, 1803738.
- [15] S. Y. Wan, Y. Li, W. Li, X. Y. Mao, C. Wang, C. Chen, J. Y. Dong, A. M. Nie, J. Y. Xiang, Z. Y. Liu, W. G. Zhu, H. L. Zeng, Adv. Funct. Mater. 2019, 29, 1808606.
- [16] K. Xu, W. Jiang, X. S. Gao, Z. J. Zhao, T. Low, W. J. Zhu, Nanoscale 2020, 12, 23488.
- [17] Y. Li, C. Chen, W. Li, X. Y. Mao, H. Liu, J. Y. Xiang, A. M. Nie, Z. Y. Liu, W. G. Zhu, H. L. Zeng, Adv. Electron. Mater. 2020, 6, 2000061.
- [18] C. Zhu, Y. Wang, F. Wang, J. Yang, X. Zhan, L. Fang, Z. Wang, J. He, Appl. Phys. Lett. 2022, 120, 083101.
- [19] R. E. Cohen, H. Krakauer, Phys. Rev. B 1990, 42, 6416.
- [20] T. Birol, Nature 2018, 560, 174.



www.advancedsciencenews.com



- [21] S. Y. Wan, Y. Li, W. Li, X. Y. Mao, W. G. Zhu, H. T. Zeng, *Nanoscale* 2018, 10, 14885.
- [22] J. Igo, S. W. Zhou, Z. G. Yu, O. P. Amnuayphol, F. Zhao, Y. Gu, J. Phys. Chem. C 2018, 122, 22849.
- [23] M. Gabel, Y. Gu, Adv. Funct. Mater. 2021, 31, 2009999.
- [24] C. J. McClellan, E. Yalon, K. K. H. Smithe, S. V. Suryavanshi, E. Pop, ACS Nano 2021, 15, 1587.
- [25] M. W. Si, A. K. Saha, S. J. Gao, G. Qiu, J. K. Qin, Y. Q. Duan, J. Jian, C. Niu, H. Y. Wang, W. Z. Wu, S. K. Gupta, P. D. D. Ye, *Nat. Electron.* 2019, 2, 580.
- [26] Q. M. Wang, L. L. Yang, S. W. Zhou, X. J. Ye, Z. Wang, W. G. Zhu, M. D. McCluskey, Y. Gu, J. Phys. Chem. Lett. 2017, 8, 2887.
- [27] S. V. Kalinin, Y. Kim, D. D. Fong, A. N. Morozovska, Rep. Prog. Phys. 2018, 81, 036502.